JACS
JOURNAL OF THE AMERICAN CHEMICAL SOCIETY

pubs.acs.org/JACS
Article

Identification of Solid-Electrolyte Interphase Species by Joint Characterization of Li-Ion Battery Chemistry by Mass Spectrometry and Electrochemical Reaction Networks

Mona Abdelgaid, Oliver Hvidsten, Théo Sombret, Egon Kherchiche, Julien Maillard, Antonin Gajan, Patrick Bernard, Kamila Kaźmierczak, Mauricio Araya-Polo, Germain Salvato Vallverdu, Carlos Afonso, Pierre Giusti, and Kristin A. Persson*

Cite This: https://doi.org/10.1021/jacs.6c04755

Read Online

ACCESS | Metrics & More | Article Recommendations | Supporting Information

ABSTRACT: The formation and stability of the solid-electrolyte interphase (SEI) play central roles in determining the long-term performance and safety of modern electrochemical energy storage systems. Despite decades of research, the SEI's heterogeneous, dynamic, and multiphase nature has defied comprehensive molecular-level characterization, creating a critical knowledge gap that limits rational battery design. In this work, we introduce a computational−experimental framework that integrates high-throughput quantum chemistry calculations, data-driven electrochemical reaction networks (eCRNs), stochastic algorithms, and laser desorption/ionization Fourier transform ion cyclotron resonance mass spectrometry (LDI-FTICR-MS) to unravel SEI formation in carbonate-based electrolytes without imposing predefined mechanisms. We constructed the most comprehensive eCRN to date, spanning over 10,000 species and 209 million reactions. Through stochastic network analysis, we successfully recovered 27 species that were previously reported in the literature and predicted 28 novel SEI species—nearly doubling our scientific knowledge in this area. Each new species was rigorously confirmed through advanced mass spectral analysis of its distinct molecular and isotopic signatures. We kinetically refined the formation pathways for a select set of both previously reported and novel SEI products, revealing kinetically feasible elementary reaction mechanisms with activation barriers below 1 eV. This computational−experimental approach deepens our molecular-level understanding of SEI chemistry by resolving which species form and through which decomposition mechanisms they emerge. Such knowledge provides the foundation necessary to connect electrolyte composition to the resulting SEI components, a critical step toward a more informed electrolyte development in next-generation lithium-based batteries.

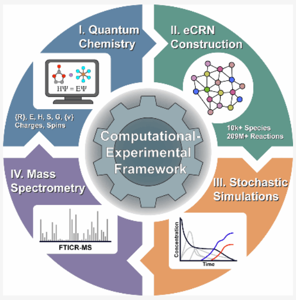

■ INTRODUCTION

Rechargeable batteries form the backbone of contemporary energy storage technologies and lithium-ion batteries in particular power devices ranging from portable electronics to electric vehicles and large-scale energy systems.[1,2] However, pushing the boundaries of electrochemical energy storage performance, safety, and longevity demands a deeper understanding of the diverse set of reactions that occur at the electrode−electrolyte interface, many of which contribute to the formation of the solid-electrolyte interphase (SEI).[3,4] The SEI was introduced by Peled[5] in 1979 as an electronically insulating and ionically conducting passivation layer, formed as a result of electrolyte reduction under the highly reducing conditions near the anode during the first cycles.[6,7] Without the SEI, uncontrolled electrolyte breakdown reactions lead to rapid capacity loss, poor Coulombic efficiency, and eventual battery failure.[7] Early models offered a biphasic view of the SEI, composed of a stable inorganic inner layer in contact with the anode and a more organic, solvent-rich outer layer facing the electrolyte.[8] To this day, the SEI continues to be considered "the most important but least understood (component) in rechargeable Li-ion batteries"[9] due to the complex nature of the spontaneous chemical and electrochemical processes involved in its formation and the lack of adequate direct characterization of its physical properties.[6,10] Its structure, morphology, composition, and properties are highly sensitive to many factors, including electrolyte components, electrode materials, solvents, additives, temperature, and areal current.[11]

Historically, much of what is known about the SEI has come from bulk or ensemble-averaged analytical methods such as X-ray photoelectron spectroscopy (XPS),[12] scanning electron microscopy (SEM),[13] X-ray diffraction (XRD),[13] Fourier transform infrared spectroscopy (FTIR),[14] time-of-flight secondary ion mass spectrometry (ToF-SIMS),[15] and others.[16,17] While these analytical techniques have been essential

Received: March 4, 2026
Revised: March 25, 2026
Accepted: March 31, 2026

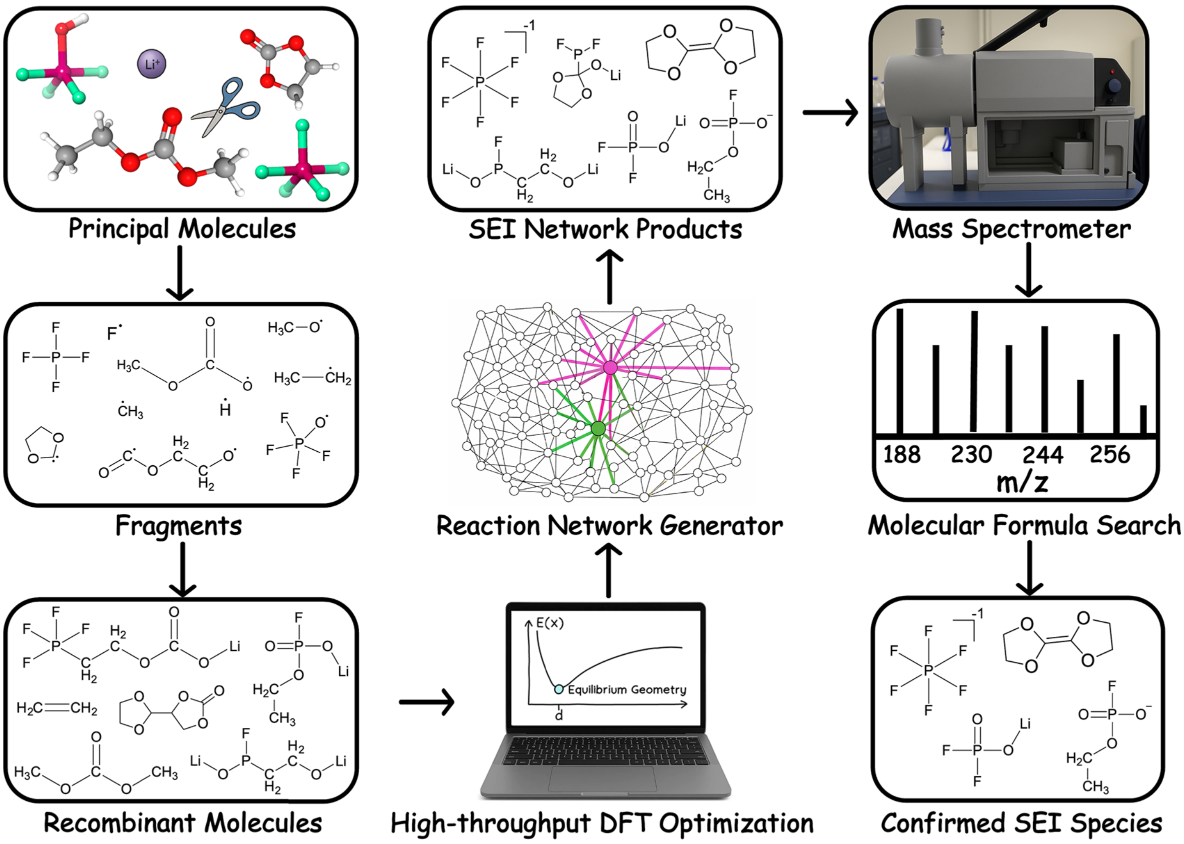

Figure 1. Workflow illustrating the fragmentation of the principal molecules and the further recombination of these fragments to form new, larger molecules. All molecules are then analyzed using high-throughput DFT calculations, which provide an understanding of their 3D geometry, thermodynamic quantities (e.g., energy, enthalpy, and entropy), and vibrational frequencies. These properties are then filtered and enumerated to generate electrochemical reaction networks and stochastically identify key network species using a set of heuristics. Then, the computationally identified species are experimentally confirmed through mass spectral analysis of molecular and isotopic signatures.

in shaping our current understanding, they each provide partial insight into the SEI's complex structure and chemistry. Electron microscopy and diffraction-based approaches like SEM and XRD excel at revealing surface morphology, cross-sectional structure, and crystalline phase information, yet they face significant challenges in directly probing the chemical bonding environment and molecular-level interactions within the SEI.[18,19,13] XPS, on the other hand, has been widely used to analyze surface composition and identify key SEI species (e.g., lithium fluoride (LiF), lithium carbonate (Li_2CO_3), and organic compounds) with nanoscale spatial resolution.[17,20] Despite its sensitivity, the poor electronic conductivity inherent to the SEI creates substantial difficulties during measurement, as charging effects during standard XPS analysis result in binding energy shifts that are notoriously difficult to calibrate and correct.[17,18,20] Moreover, the coexistence of multiple lithium-containing compounds and multilayer SEI architecture that varies spatially across the electrode surface further limits the accuracy and interpretability of these traditional approaches. Importantly, distinguishing organic from inorganic layers presents acute analytical difficulties. FTIR spectroscopy has become the primary tool for evaluating the organic SEI and electrolyte chemistry due to the many IR-active vibrational modes of both salts and carbonate solvents comprising the electrolyte and its decomposition products.[14] However, FTIR analysis faces significant practical limitations, including inherent sensitivity constraints, complex sample handling requirements, and susceptibility to environmental interference.[16,17]

To precisely determine the molecular composition of the SEI on the anode surface, advanced high-resolution mass spectrometry, particularly Fourier transform ion cyclotron resonance mass spectrometry (FTICR-MS), offers a powerful approach.[21−24] This technique provides exceptional mass resolution, capable of distinguishing between species that differ by less than the mass of an electron,[24] and delivers mass accuracy sufficient to assign distinct molecular formulas to each detected signal.[23] Such precision makes it particularly effective for identifying unknown compounds in complex chemical systems.[23] FTICR-MS also features a broad dynamic range, allowing the detection of trace-level species and isotopic variants critical for confident molecular identification.[25] When combined with laser desorption/ionization (LDI), it further enables spatially resolved surface analysis, facilitating detailed mapping of the SEI's molecular heterogeneity.[26,27]

Recent studies have demonstrated the remarkable capabilities of FTICR-MS in advancing molecular-level insight into the SEI and electrolyte chemistry. Using matrix-assisted FTICR-MS and ToF-MS, Sombret et al. monitored the degradation behavior of various lithium salts under controlled and air-exposed conditions, showing that electrolytes in the solid state remained chemically stable for over 24 h, in contrast to the rapid degradation observed in solution.[28] Maillard et al. utilized the LDI-FTICR-MS method to analyze SEI composition and identified degradation products from both salt and solvent decomposition.[27] The high elemental diversity (C, H, O, Li, P, F) led to over 4,000 signals per electrode in each ionization mode, making manual assignment extremely challenging.[27] This highlights the need for combining high-quality characterization with data-driven approaches that leverage first-principles calculations and computational electrochemical reaction networks (eCRNs) to aid in the identification of SEI components.[29−31]

To bridge this gap, Persson and co-workers developed the first scalable computational frameworks to explore complex electrochemical reaction networks.[29−32] Xie et al. applied graph-based models and shortest-path algorithms to identify the formation pathways for key SEI products.[29] Barter et al. introduced the high-performance reaction generation method, which leverages filter-based reaction enumeration and stochastic analysis, to recover known SEI products and identify previously unrecognized SEI species.[30] Using kinetic Monte Carlo (kMC) simulations informed by automated eCRN analysis and ab initio calculations, Spotte-Smith et al. explored SEI formation and evolution of the solvent decomposition, revealing the mechanistic origins of the Peled-like bilayer interphase structure on the negative electrode of Li-ion batteries.[31] Such kMC approaches are increasingly recognized as essential tools for bridging molecular-scale phenomena with macroscopic battery models, offering the computational accuracy needed to understand complex electrochemical reactions and evolving solid interfaces.[33] By combining first-principles and data-driven simulations with microkinetic models, it is now possible to rapidly generate hypotheses for experimental characterization and in-depth mechanistic studies of complex reactive processes. However, notably, no eCRN has yet been constructed that simultaneously captures both salt and solvent decomposition along with their joint products. This limitation has precluded the data-driven identification of hybrid species, such as fluorinated organophosphate carbonates, that arise from coupled solvent−salt decomposition and therefore incorporate both P/F centers and carbonate moieties.

In this work, we combine LDI-FTICR-MS with quantum chemistry calculations, data-driven electrochemical reaction networks, and stochastic simulations to characterize an SEI formed on a graphite anode in a typical carbonate-based LIB electrolyte, as shown in Figure 1. The ultrahigh-resolution LDI-FTICR-MS technique identified over 30,000 signals for the formation cycle for $S/N > 3$, which include multiple isotopic and ionic variants of key SEI species. Bridging this experimental richness with theoretical prediction, we constructed and analyzed a massive-scale electrochemical reaction network, including both salt and solvent reactivity, to systematically generate candidate SEI species for direct comparison with LDI-FTICR-MS. We recovered 27 known SEI components and identified 28 novel species previously unreported in the literature. Additionally, we identified kinetically feasible pathways for the formation of a representative set of these novel SEI species. Together, these elements of the study provide information on the existence of previously unidentified species, which is key for the development of system-scale SEI modeling, and reinforce the critical advantage of coupling theoretical and experimental approaches to characterize the SEI.

■ EXPERIMENTAL METHODS

Electrolyte Preparation

The study was carried out on a negative electrode coming from batteries filled with an electrolyte composed of highly pure $LiPF_6$ (purity > 99.5%, supplied by Soulbrain) and battery-grade solvents ethylene carbonate (EC) and ethyl methyl carbonate (EMC) (both provided by Capchem, purity > 99.5%): 1 M $LiPF_6$ in EC/EMC (30/70) vol. The electrolyte was prepared under an argon atmosphere in a glovebox and stored in airtight aluminum containers. All compounds used for the electrolyte formulation were placed in a drying oven overnight. Before use, the spatulas were cleaned with dimethyl carbonate (DMC, >99.5% pure, supplied by Capchem). After formulation, the electrolyte was left in the glovebox overnight before use to ensure the complete dissolution of the lithium salts.

Assembling, Electrochemical Tests, and Dismantling of the Cells

Single-layer pouch cells were assembled in a dry room (dew point below −45 °C), with a negative electrode of 2.74 × 2.74 cm^2 and a positive electrode of 2.54 × 2.54 cm^2. The active materials of the negative and positive electrodes were graphite and lithiated lamellar oxide $LiNi_{0.6}Mn_{0.2}Co_{0.2}O_2$ (NMC 622), respectively. The electrodes were all provided by Saft company. A Celgard 2325 type separator was placed between the two electrodes. After assembly, the cells were left to dry at 80 °C in a vacuum chamber for at least one night. Once dried, the pouch cells were filled with the electrolyte and sealed in a glovebox before cycling. Electrochemical analyses were performed using a BioLogic BCS-805 battery cycler. All of the cycles were performed using a constant current mode between 2.7 and 4.2 V. All of the cells only underwent a cycle at a C-rate of C/20−D/20 at 60 °C. The objective of this cycle is to study the initial formation of SEI. The cells were disconnected immediately after this first cycle. Pouch cells were then recovered and dismantled in an Ar-filled glovebox. The electrodes were washed in EMC two times in aluminum cups for 30 s. The objective was to remove, before analysis, the Li-salt possibly trapped in the electrode pores. Once washed, the electrodes were dried at room temperature in the glovebox before further handling. The porous separator containing the electrolyte was also placed in a few milliliters of the EMC solvent to recover the degraded electrolyte trapped in the pores of the separator. All of the electrochemical data are presented in Figure S1 and Table S1.

Mass Spectrometry Procedure

Mass spectrometry analyses were conducted using a FTICR-MS equipped with an 18 T superconducting magnet (MRMS, Bruker Daltonics, Bremen, Germany) equipped with a laser desorption ionization source with a Nd:YAG × 3 laser at 355 nm. Prior to analysis, the electrodes were attached to a stainless steel MALDI plate with a conductive aluminum adhesive tape. All sample handling, including electrode preparation and deposition, was performed under an argon atmosphere in a glovebox (O_2, H_2O < 0.8 ppm) to avoid oxidation or moisture contamination. The samples were transferred from the glovebox to the mass spectrometer source in a plastic zip bag filled with N_2 gas to avoid contact with air.[27] The mass spectra were acquired in positive mode in the m/z range 90−1000. Conditions were optimized to afford the transmission of low m/z ions: plate offset 100 V; deflector plate 220 V; Funnel 1 RF 150 V_{pp}, Funnel 2 RF 150 V_{pp}; multipole RF 200 V_{pp}; ToF 0.500 ms; collision cell RF 650.0 V_{pp}, RF amplitude 350 V_{pp}, RF frequency 6 MHz, chirp excitation power 25%; and number of scans 50. The source parameters were set up as follows: laser frequency 10,000 Hz, laser focus small, laser power 35%, and number of shots by burst 680. The analog time domain signal was digitalized using 8 million data points, apodized, and zero-filled once before Fourier transform. With a low acquisition mass of m/z 90, this resulted in a time domain signal of 1.4 s yielding a mass spectrum with a resolving power of 700,000 at m/z 200 (magnitude mode and 1ω detection). The analyses were performed on four graphite negative electrodes after the formation cycle. The mass spectra are presented in Figure S2. To assess the persistence of the identified SEI species under prolonged electrochemical operation, we performed a mass spectrometric analysis of graphite electrodes harvested from pouch cells after 250 cycles. The electrochemical cycling data up to 250 cycles together with the corresponding high-resolution LDI-FTICR-MS spectrum are presented in Figure S3.

Molecular formulas and data processing were performed using DataAnalysis version 6.1 (Bruker). Mass spectra were internally calibrated with carbon cluster cations coming from the graphite electrode surface. The molecular formula assignment of the species was realized with the SmartFormula tool. A tolerance of 0.5 ppm was allowed to the identification with the following elemental constraints: C_{0-50}, $H_{0-100,}$ O_{0-20}, N_0, F_{1-5}, Li_{1-5}, P_{1-5}. In many cases, owing to the high number of elements to consider, several molecular formulas were obtained with a 0.5 ppm mass tolerance. Discrimination between them was carried out by considering the isotopic fine structure with the mSigma score given by the DataAnalysis SmartFormula tool and manual control.

■ COMPUTATIONAL METHODS

Data Generation through Fragmentation and Recombination

The set of possible species that could contribute to the SEI formation in LIBs was generated by fragmenting the principal molecules, including the solvent molecules (e.g., EC and EMC), salts (e.g., $LiPF_6$), and one of the early salt decomposition products (e.g., PF_4OH). Importantly, PF_4OH was included in the initial state, thereby ensuring representation of concerted salt decomposition mechanisms such as the $PF_5{-}Li_2CO_3$ adduct dissociation to LiF, CO_2, and $LiPOF_4$.[34] This approach ensures that the combined chemical space spanning both salt-derived (P, F) and solvent-derived (C, H, and O) fragments is accessible during recombination, enabling the formation of hybrid species that would be impossible through separate decomposition pathways. We implemented a systematic two-step fragmentation approach. The first step involved systematic breaking of bonds within each principal molecule to generate an initial set of molecular fragments. In the second step, these fragments were further fragmented, producing a broader and more diverse pool of smaller molecular units. Following this hierarchical fragmentation, these fragments were allowed to selectively recombine to form larger molecules. This combination of sequential fragmentation and strategic recombination yielded a chemically diverse set of species that could serve as intermediates connecting original electrolyte components to the final SEI products. All principal molecules, fragments, and recombinant molecules were optimized using high-throughput density functional theory (DFT) calculations, which provide an understanding of their 3D geometry, thermodynamic quantities (including total electronic energy, enthalpy, entropy, and Gibbs free energy), and vibrational frequencies. Following molecule generation and analysis, the resulting data set was then augmented with molecules from the lithium-ion battery electrolyte data set[35] that fell into three categories: those containing C, H, O, and/or Li; those containing P, F, and/or Li or H; and those containing P, F, C, H, O, and/or Li. This workflow enabled a comprehensive exploration of the complex reactive landscape governing LIB electrolyte chemistry.

Density Functional Theory

DFT calculations were performed using the Q-Chem electronic structure package.[36] Geometry optimizations for all species within the reaction network utilized the range-separated hybrid functional ωB97X-V[37] in conjunction with the triple-ζ def2-TZVPPD[38] basis set, which incorporates diffuse and polarization functions for improved accuracy in noncovalent interactions. Solvation effects were incorporated implicitly via the SMD continuum solvation model,[39] parametrized to emulate a lithium-ion battery electrolyte environment. A dielectric constant of $\varepsilon = 18.5$ was selected to approximate the permittivity of a 3:7 (v/v) EC:EMC solvent mixture, while remaining solvent descriptors (e.g., surface tension, atomic radii) were retained at values corresponding to pure ethylene carbonate to maintain consistency with prior studies.[35]

Transition state (TS) structures were initially located using the automated AutoTS[40] protocol within the Jaguar[41] software package, employing the ωB97X-D functional[42] paired with the split-valence def2-SVPD basis set[38,43] and the C-PCM[44] implicit solvation model to balance computational efficiency and reliability for saddle-point searches. TSs that were unable to be identified via this procedure were manually estimated and optimized by Jaguar's built-in TS optimization methods. To ensure robust characterization, all TS candidates were rigorously validated by (1) confirming the presence of a single imaginary vibrational frequency corresponding to the reaction coordinate and (2) performing intrinsic reaction coordinate (IRC)[45] analyses to verify connectivity between reactant and product minima. Final TS geometries and energies were recalculated at the higher-level ωB97X-V/def2-TZVPD/COSMO[46] theory to provide more accurate reaction energy profiles.

Electrochemical Reaction Network Generation

To construct the electrochemical reaction network, we first applied a filtering methodology.[30] Starting with a data set of 23,625 candidate species, we applied a series of systematic filters to eliminate species that are chemically unreasonable or undesirable under the conditions studied. The framework then enumerates all stoichiometrically valid reactions and employs user-defined criteria to eliminate reactions based on physical or practical criteria, while preserving a chemically diverse and meaningful reaction network. A detailed description of species and reaction filters employed in this work can be found in Barter and coworkers.[30]

Stochastic Simulations

We employed the Reaction Network Monte Carlo (RNMC) framework developed by Zichi et al.,[47] which leverages a scalable, parallel implementation of Gillespie's direct method[48] with significant optimizations for handling massive reaction networks. Specifically, we employ kMC simulations as a stochastic sampling framework to identify which reactions occur and which species form via multiple reaction pathways, emerge most readily, and persist without being consumed. While this approach has proven an excellent method to identify SEI species,[29−31] we emphasize that it does not provide reaction time scales or quantitative product distributions. Building on that foundation, we performed 50,000 kMC simulations in parallel under 0.0 V vs Li/Li^+ and 298.15 K, designed to probe the stochastic evolution of complex reactive systems. In order to efficiently estimate the system's species dynamics, each simulation was initialized with a representative electrolyte composition of 30 Li^+, 30 PF_5, 30 PF_4OH, and a solvent mixture of 30 molecules split between EC and EMC in a 30:70 volumetric ratio (12 EC and 18 EMC). In addition, the system is treated within the grand-canonical ensemble with the anode acting as an electron reservoir, enabling control of the voltage via the electron chemical potential. PF_4OH was included in the initial state to circumvent reaction filters that exclude reactions involving more than two simultaneous bond breakages/formations, thereby ensuring representation of concerted salt decomposition mechanisms such as the $PF_5{-}Li_2CO_3$ adduct dissociation to LiF, CO_2, and $LiPOF_4$.[34] In addition, more computationally intensive simulations were initialized with a "true-to-experiment" composition of 10,908 molecules of EC, 16,395 molecules of EMC, and 2,697 molecules of the salt. This represents a volume of 4500 nm^3 with an approximate 1 M of $LiPF_6$ concentration in 30:70 EC:EMC. For the smaller electrolyte system, 30 molecules of each major component were sufficient to adequately sample the system's reactive behavior while maintaining computational tractability, providing statistically meaningful results through the ensemble of thousands of parallel simulations.

In these kMC simulations, the system evolved stochastically from the defined initial state with reaction events selected probabilistically based on the supplied rate coefficients. Given the scale of the reaction network, which entails millions of reactions, it is computationally infeasible to assign accurate, individually calculated rate constants. To address this, we employed uniform rate coefficients: all unimolecular reactions were assigned a constant rate of k_0, while bimolecular reactions were assigned a rate of k_0/V, where V is the system volume introduced to maintain correct dimensionality. Specifically, we calculated rate constants using transition state theory:

$$k = \frac{k_B T}{h} \cdot e^{(-\Delta G^{\ddagger}/k_B T)}$$

where k_B is the Boltzmann constant, h is the Planck constant, T is the temperature, and $\Delta G^{\ddagger}$ is the activation energy barrier. We used a systematic barrier construction where $\Delta G^{\ddagger}$ = constant barrier for

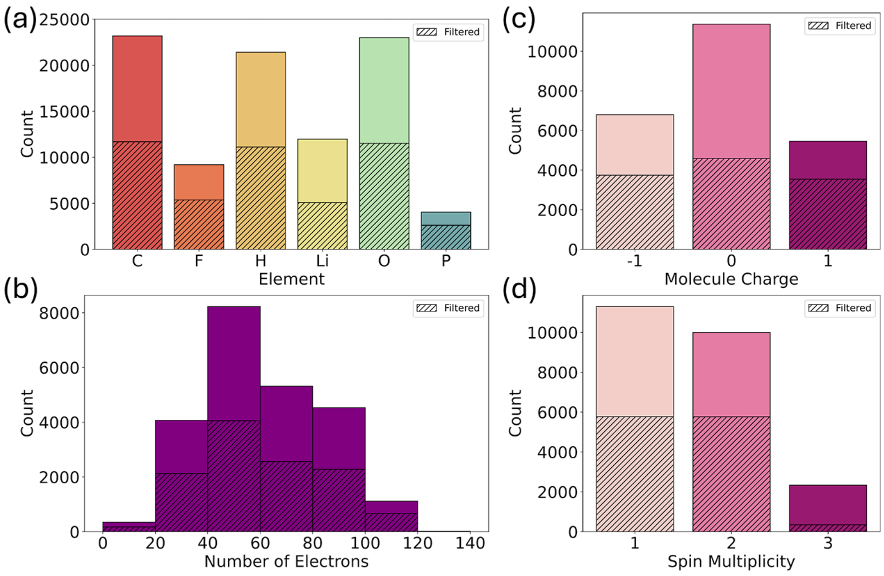

Figure 2. Analysis of the composition of the data set used to construct the eCRN. Each plot includes a solid-colored bar representing counts in the original data set fed to the filtering framework and a hatched overlay bar for the filtered subset. (a) Number of unique molecules containing each elemental species; (b) distribution of molecules by number of electrons; (c) number of molecules with formal charges of −1, 0, and +1; and (d) number of molecules with spin multiplicity values of 1, 2, and 3.

exergonic reactions and $\Delta G^{\ddagger} = \Delta G_{\text{reaction}}$ + constant barrier for endergonic reactions. This approach enables consistent and tractable sampling of the reaction network while preserving the relative dynamics between uni- and bimolecular processes. With sufficient sampling, all reactions represented in the network that would occur under accurate kinetics are captured in kMC simulations with fixed rate coefficients. Previous computational studies of chemical reaction networks relied on simplified approaches, such as Stocker et al. combustion network analysis, which utilized reaction thermodynamics coupled with arbitrary energy barriers to explore network dynamics.[49] Additionally, Spotte-Smith and co-workers successfully recovered experimentally observed SEI products without knowledge of reaction kinetics, showing that reaction thermodynamics alone can be sufficient to predict reasonable reaction pathways as well as SEI network products.[30] Furthermore, Blau et al. demonstrated using a 6,000-species eCRN that thermodynamic-driven analysis can autonomously identify viable reaction pathways, recovering all known formation mechanisms for lithium ethylene dicarbonate while discovering three additional novel routes.[32]

RESULTS AND DISCUSSION

We generated a comprehensive eCRN aimed at capturing the formation of the SEI in LIBs. The initial data set comprises 23,625 species with varying charges (−1, 0, +1) and spin multiplicities (1, 2, 3), as shown in Figure 2. The data set was biased toward the C−H−O−Li chemical system because most principal molecules are organic in nature, with 4,053 phosphate-containing molecules present as well. The bonding motifs observed for phosphorus were limited (only F−P and O−P, while a small number of C−P, H−P, and Li−P bonds were also present) because these molecules are all derived from salt and solvent joint decomposition products. Furthermore, we examined the molecular size distribution based on electron count and observed that while the majority of species are relatively small molecules, the data set includes a subset of considerably larger molecules compared to the original electrolyte solvent molecules and salt anions, containing up to 120 electrons. While the data set is intentionally biased toward smaller molecular species (e.g., only one recombination step of the molecular fragments) due to the high computational cost of larger molecules, it effectively addresses the core chemical processes governing SEI formation and provides a robust foundation for future extensions to larger molecular systems.

To refine the data set, we implemented a number of user-defined filters (summarized in the Supporting Information) to remove undesirable species, yielding a set of 11,867 filtered species. These filtered species were then organized into composition-based groups, where each group contains entries consisting of either a single molecule or a pair of molecules whose combined composition matches that of the group. Across all groups, we generated every stoichiometrically valid reaction and filtered them using physical and practical criteria, yielding 208,929,658 reactions—the largest eCRN for LIB SEI formation to date (Figure S4) and the first to include coupled salt−solvent decomposition pathways.

To analyze the eCRN, we performed thousands of parallel kMC simulations, with each simulation producing distinct reaction trajectories that collectively map the complex reactive landscape of the SEI formation. These trajectories enable two complementary analysis approaches, including targeted pathway discovery and autonomous product identification. For known species of interest, we trace trajectories to identify the shortest reaction pathways leading to their formation and rank these pathways using cost functions. For unbiased product discovery, we apply heuristic criteria across all trajectories to identify likely network products. Species qualify as network products if they: (i) are formed substantially more than they are consumed (ratio of producing reactions to consuming reactions >1), (ii) cumulate to a significant degree on average (average final concentration must be >0.1), and (iii) are accessible through low-cost pathways (number of elementary steps from initial species to the final product <15). It is important to note that the identified network products do not necessarily represent the metastable or stable species that would be observed experimentally in the SEI, nor are they necessarily exhaustive, as they depend on which species are included in the eCRN construction, the chosen threshold parameters, and the initial conditions of the kMC simulations. Rather, the network

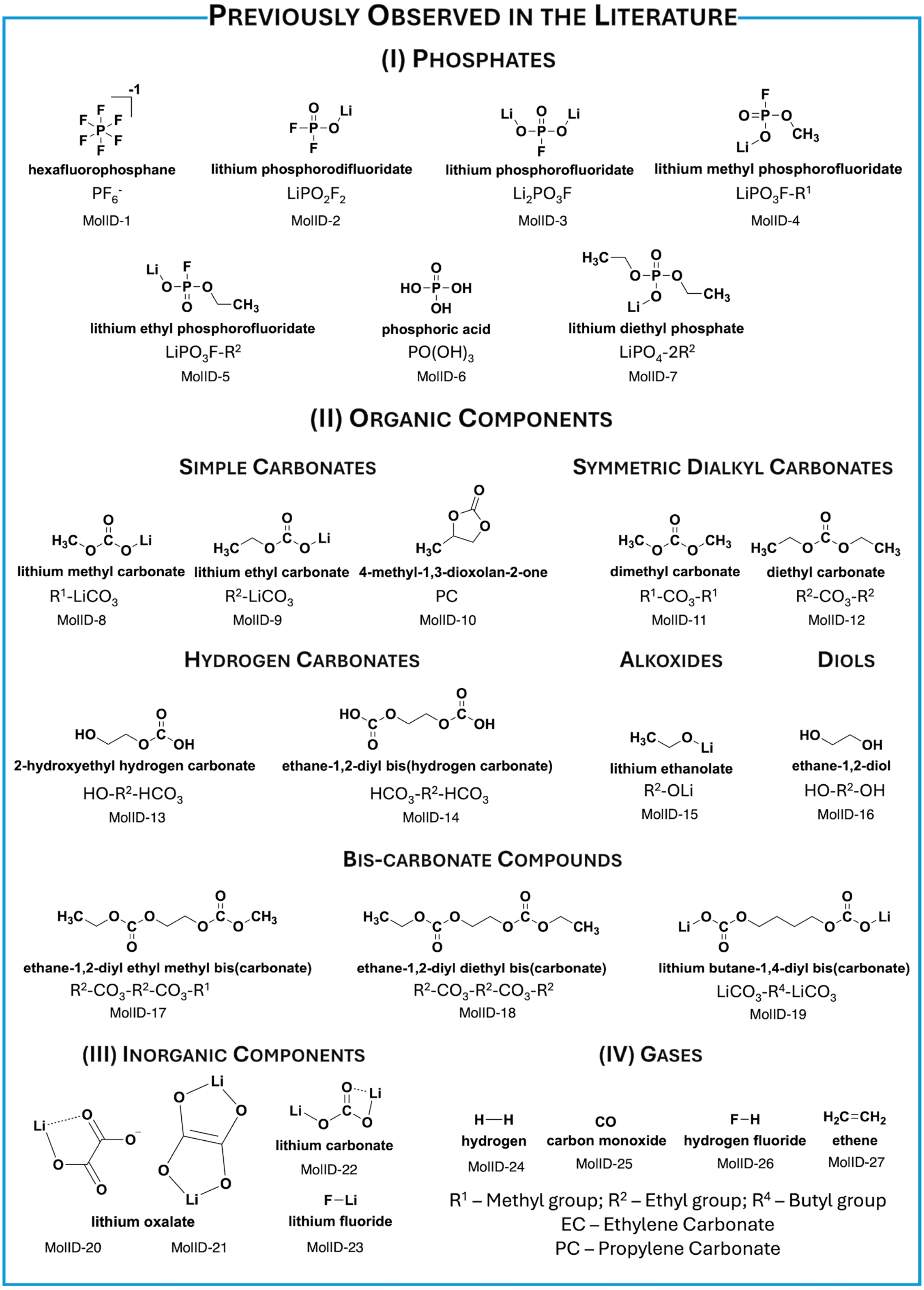

Figure 3. Stochastic network analysis recovered 27 species that have been reported in the SEI literature. These species include major gases, inorganic molecules, linear alkyl carbonates, and phosphate derivatives.

products serve as valuable hypotheses for species that might form in actual reactive systems, which can subsequently be validated experimentally using techniques such as ultrahigh-resolution LDI-FTICR-MS.

The utility of our approach was evaluated through the analysis of a diverse set of network products (predominantly neutral molecules with a smaller subset of anions) generated under various initial kMC conditions, as described in the methodology section. To search for these molecules in LDI-FTICR-MS spectra in positive and negative ionization modes, we developed a Python code that systematically generates all relevant ionic forms for each molecule. For the positive ionization mode,

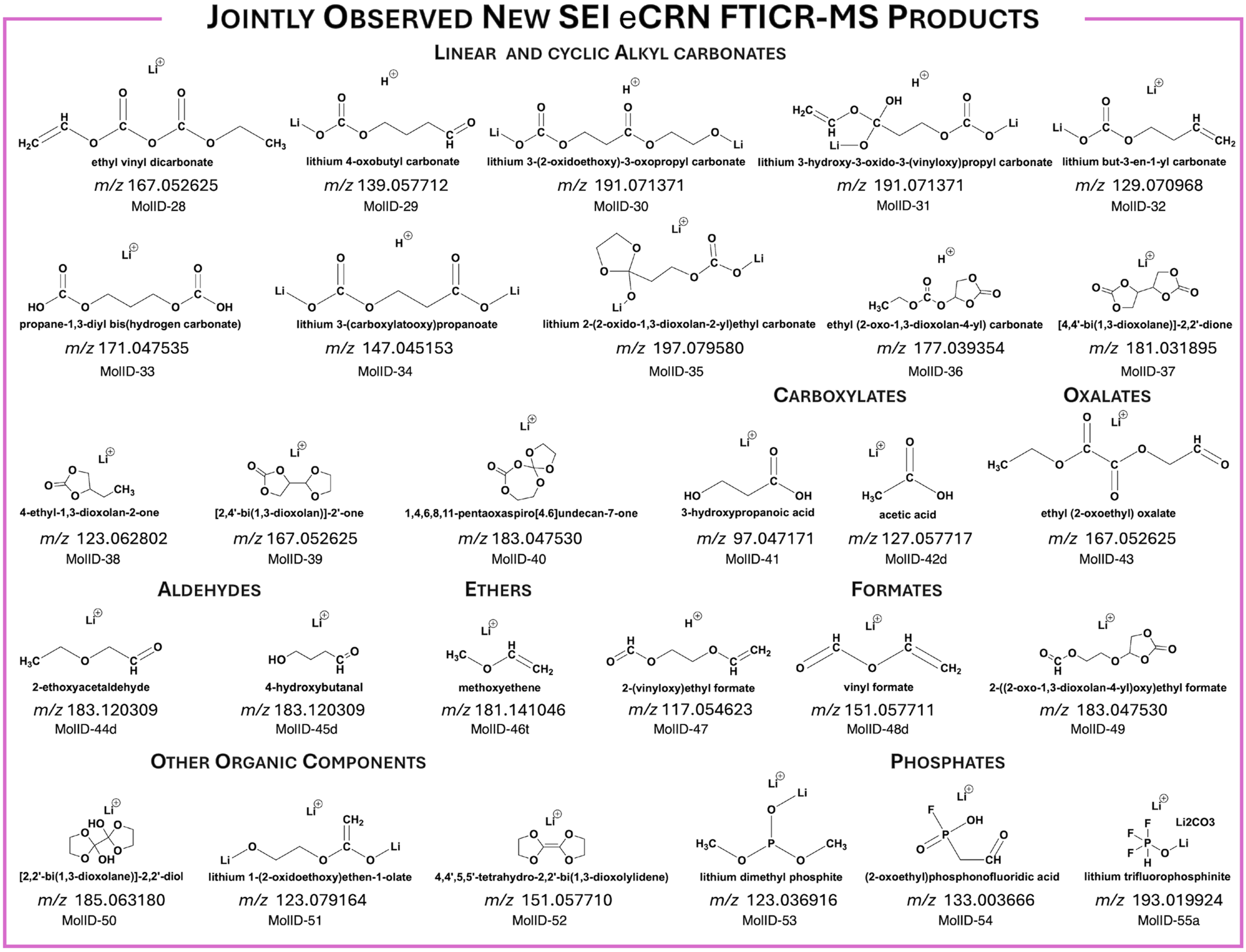

Figure 4. Novel SEI species discovered through integrated eCRN and kMC simulations and LDI-FTICR-MS validation. These molecules, organized by structural motifs, represent a major expansion of SEI chemistry and demonstrate the predictive power of network-based theoretical approaches when coupled with high-resolution mass spectrometry validation. The exact experimental *m*/*z* of each ion is shown with a hierarchical detection priority: monomer masses are displayed first when detected; if the monomer is not detected but a dimer is found, the dimer mass is shown (marked with "d"); and if neither monomer nor dimer is detected, the trimer mass is displayed (marked with "t"). MolID-55 with an exact mass followed by "a" indicates that this species was only detected with a Li_2CO_3 adduct.

network products were cationized by adding Li^+ or H^+, while in the negative mode, we searched for their deprotonated and Li^+-deficient counterparts. The algorithm incorporates common adduct formations by combining the base molecular formula of the monomer species with an adduct (LiF or Li_2CO_3), followed by ionization with either Li^+ or H^+. Additionally, we generated the corresponding dimeric and trimeric species to account for potential aggregation effects. For every candidate ion, we calculated the exact mass of both the parent ion and its isotopic variants. Species confirmation requires the detection of the signal corresponding to both the parent ion and its expected isotopic peaks in LDI-FTICR-MS. This systematic ion generation and matching pipeline enabled robust cross-checking between the reaction network predictions and LDI-FTICR-MS, revealing several previously unreported species (Table S2).

Our computational approach recovered 27 SEI products that are previously reported in the literature (Figure 3). These include (i) gases such as H_2, C_2H_4, and CO;[50] (ii) inorganic species including inorganic carbonates (e.g., Li_2CO_3), lithium oxalate ($Li_2C_2O_4$), and LiF;[51−53] (iii) organic species like lithium methyl carbonate (LMC),[54,55] lithium ethyl carbonate (LEC),[55] lithium butylene dicarbonate (LBDC),[52] ethane-1,2-diyl diethyl biscarbonate,[56] to name a few; and (iv) phosphate compounds[27,34] such as hexafluorophosphate (PF_6^-), lithium phosphorodifluoridate ($LiPO_2F_2$), lithium phosphorofluoridate (Li_2PO_3F), phosphoric acid (H_3PO_4), and others. It should be noted that LDI-FTICR-MS has inherent limitations in detecting very low molecular weight and volatile species (e.g., CO, C_2H_2, Li_2CO_3, etc.) due to their poor retention during the desorption process and the low mass detection limits of the technique. Overall, the successful recovery of these well-known SEI species demonstrates the robustness of our computational approach, particularly considering that reaction kinetics are entirely ignored in network exploration.

Most remarkably, our computational framework uncovered several novel products that have not previously been proposed to participate in SEI formation (Figure 4). These molecules were further experimentally confirmed through mass spectral analysis of the molecular and isotopic signatures, as depicted in Figure 5. These 28 unique species include fluorinated organophosphate-

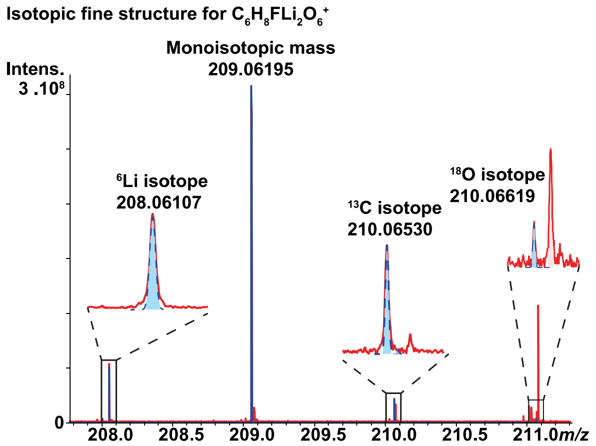

Figure 5. MALDI(+) FTICR MS of a negative electrode showing the isotopic fine structure validation of the $C_6H_8FLi_2O_6^+$ ion (MolID-40 with the LiF adduct) with the ^{6}Li, ^{13}C, and ^{18}O isotopes showing perfect matching in mass and intensity between the experimental mass spectrum (in red) and the theoretical profile in blue.

carbonates, cyclic and bicyclic alkyl carbonates, oxalates, formates, diols, ethers, aldehydes, carboxylates, and dioxolanes. Critically, the SEI is known to evolve dynamically during battery aging. However, the decomposition products identified in this work are not limited to short-lived, early-stage intermediates. Rather, our combined computational and experimental analysis shows that these species constitute persistent and structurally significant components of the SEI architecture. Table 1 shows the exact masses of species detected in both the freshly formed SEI and after 250 cycles, confirming that most of our predicted species remain detectable after extended cycling. Specifically, 25 of the 28 molecules listed in Figure 4 are observed (under at least one ionic form, as shown in Table S2) with sufficient signal intensity after 250 cycles, and 2 additional species remain detectable at low intensity after 250 cycles. Only lithium dioxolane-ethyl carbonate, LDEC (MolID-35), is no longer observed after long-term cycling. It should be noted that among the four species marked as not detected (ND) in the aged SEI, three were successfully detected in an alternative ionic form, as highlighted in Table S2. Likewise, MolID-51 was detected with a sufficient signal intensity in a different ionic form. In addition, Figure 6 depicts two representative examples (MolID-50, MolID-54) for which we provide zoomed-in FTICR-MS peak regions extracted from both the freshly formed and the aged SEI spectra. These analyses show that the same molecular ions (within subppm mass accuracy) are consistently detected before and after long-term cycling, reinforcing the persistence and

Table 1. MALDI (+) LDI-FTICR-MS Molecular Assignment with Theoretical Exact Mass, Experimental Measurement (for Both Formed and Aged SEI), and Relative Error for All of the New Molecular Formulas Found on the Mass Spectra[a]

MolID #	Ion molecular formula	Theoretical *m/z*	Formed SEI experimental *m/z*	Formed SEI relative error	Aged SEI experimental *m/z*	Aged SEI relative error
MolID-28	$C_6H_8LiO_5^+$	167.052628	167.052625	−0.02	167.052630	0.01
MolID-29	$C_5H_8LiO_4^+$	139.057714	139.057712	−0.01	139.057713	−0.01
MolID-30	$C_6H_9Li_2O_6^+$	191.071371	191.071372	0.00	ND	
MolID-31	$C_6H_9Li_2O_6^+$	191.071371	191.071372	0.01	ND	
MolID-32	$C_5H_7Li_2O_3^+$	129.070977	129.070968	−0.07	129.070972	−0.04
MolID-33	$C_5H_8LiO_6^+$	171.047543	171.047535	−0.05	171.047532	−0.06
MolID-34	$C_4H_5Li_2O_5^+$	147.045157	147.045153	−0.03	147.045141 (LoI)	−0.11
MolID-35	$C_6H_8Li_3O_6^+$	197.079550	197.079580 (LoI)	0.15	ND	
MolID-36	$C_6H_9O_6^+$	177.039364	177.039354	−0.06	ND	
MolID-37	$C_6H_6LiO_6^+$	181.031893	181.031895	0.01	181.031895 (LoI)	0.01
MolID-38	$C_5H_8LiO_3^+$	123.062799	123.062802	0.02	123.062801	0.02
MolID-39	$C_6H_8LiO_5^+$	167.052628	167.052625	−0.02	167.052630	0.01
MolID-40	$C_6H_8LiO_6^+$	183.047543	183.047530	−0.07	183.047529	−0.08
MolID-41	$C_3H_6LiO_3^+$	97.047149	97.047171	0.23	97.047158	0.09
MolID-42d	$C_4H_8LiO_4^+$	127.057714	127.057717	0.02	127.057717	0.02
MolID-43	$C_6H_8LiO_5^+$	167.052628	167.052625	−0.02	167.052630	0.01
MolID-44d	$C_8H_{16}LiO_4^+$	183.120314	183.120309	−0.03	183.120302	−0.07
MolID-45d	$C_8H_{16}LiO_4^+$	183.120314	183.120309	−0.03	183.120302	−0.07
MolID-46t	$C_9H_{18}LiO_3^+$	181.141049	181.141046	−0.02	181.141054	0.03
MolID-47	$C_5H_9O_3^+$	117.054621	117.054623	0.02	117.054620	−0.01
MolID-48d	$C_6H_8LiO_4^+$	151.057714	151.057711	−0.02	151.057710	−0.03
MolID-49	$C_6H_8LiO_6^+$	183.047543	183.047530	−0.07	183.047529	−0.08
MolID-50	$C_6H_{10}LiO_6^+$	185.063193	185.063180	−0.07	185.063181	−0.07
MolID-51	$C_4H_6Li_3O_3^+$	123.079156	123.079164	0.06	123.079149 (LoI)	−0.06
MolID-52	$C_6H_8LiO_4^+$	151.057714	151.057710	−0.02	151.057710	−0.02
MolID-53	$C_2H_6Li_2O_3P^+$	123.036914	123.036916	0.02	123.036916	0.02
MolID-54	$C_2H_4FLiO_3\ P^+$	133.003662	133.003666	0.03	133.003662	0.00
MolID-55	$CHF_3Li_4O_4P^+$	193.019918	193.019924	0.03	193.019930	0.06

[a] The identification parameters, after calibration on the carbon clusters, were set up as follows: allowed atoms C_n, H_{40}, O_n, N_0, F_{15}, Li_5, and P_5 with a tolerance of 0.5 ppm. The letters d and t indicate dimer and trimer, respectively, whereas ND and LoI indicate not detected in the aged SEI and detected with low intensity, respectively. Note that although four species are marked as ND in the aged SEI, three of these were detected in an alternative ionic form. Also, MolID-51 is detected with sufficient intensity but under another ionic form. Complete information on all ionic forms of the newly identified species is reported in Table S2.

https://doi.org/10.1021/jacs.6c04755

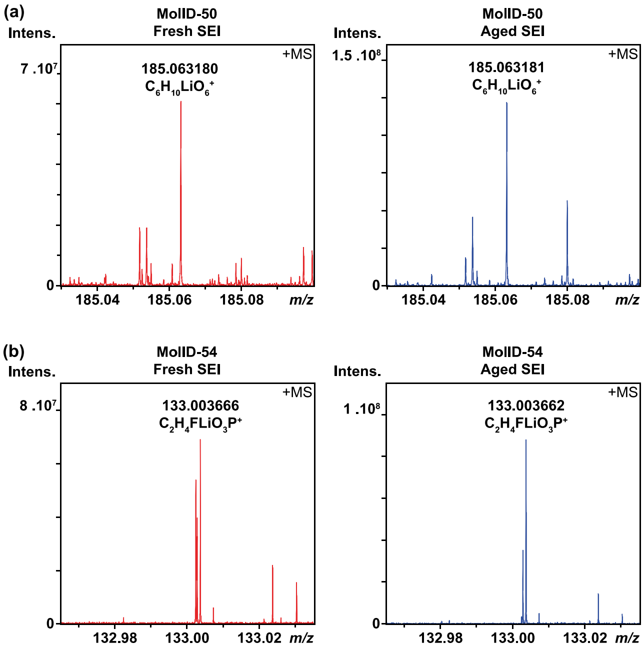

Figure 6. MALDI (+) FTICR MS assigned peaks for (a) MolID-50 and (b) MolID-54 in both fresh and aged SEI formed on negative graphite electrodes.

structural relevance of the species predicted by our computational workflow. The side-by-side analysis highlights the number of species that persist across aging and directly demonstrates the molecular overlap between the early and evolved interphase. Many of these persistent compounds, including fluorinated organophosphate-carbonates and cyclic oligomers, carry reactive functional groups that can further engage in polymerization, cross-linking, and secondary decomposition pathways. These reactivities naturally contribute to the emergence of higher mass, more complex SEI structures, also observed experimentally in the high-resolution mass spectra of the aged SEI. Thus, although the SEI becomes increasingly heterogeneous and chemically intricate with cycling, our results show that the initially formed products predicted computationally and validated experimentally remain embedded in the mature SEI architecture, acting as chemical precursors, structural motifs, or recurring fragments within the more complex interphase formed under operational conditions.

Importantly, these newly identified species have known properties that could contribute to the overall mechanical, chemical, and transport properties of the SEI. Mechanical robustness is critical for the SEI as cracking reactivates passive surfaces, significantly damaging the overall lifetime and performance of the battery.[57] Oxalates (e.g., MolID-43) can decompose preferentially during the initial battery cycles to form $Li_2C_2O_4$, which contributes to a compact, ionically conductive SEI layer with enhanced mechanical stability and reduced electrolyte decomposition.[58−60] Vinyl-bearing formates (e.g., MolID-47 and MolID-48) can undergo reductive polymerization during the initial charge cycle, forming a flexible, cross-linked polymer network within the SEI.[61−65] These vinyl-initiated radical polymerization pathways are known to generate cohesive, polymer-rich layers that enhance SEI elasticity, relieve mechanical stress, suppress dendrite growth, improve ionic conductivity, and effectively block electron tunneling.[61−65] Cyclic carbonates, particularly 1,3-dioxolane derivatives (e.g., MolID-35 to MolID-39), also undergo polymerization and decomposition to form hybrid organic−inorganic SEI layers with enhanced mechanical stability, allowing the interphase to accommodate electrode volume changes and mitigate crack propagation during lithiation/delithiation cycles.[66] The longer-chain alkyl carbonates (e.g., MolID-28 to MolID-34) and flexible ether molecules (e.g., MolID-46) could provide enhanced mechanical accommodation in SEI layers through their increased conformational flexibility. Moreover, diols (e.g., MolID-50) can act as cross-linking agents, enhancing the mechanical strength of the SEI layers in LIBs.[67,68] Chemical stability is another essential performance parameter, especially given that the SEI's primary role is surface passivation of the anode.[69] The fluorinated phosphate−carbonate hybrids[66,70,71] (e.g., MolID-53 and MolID-54) may assist in the stabilization between the organic and inorganic components of the SEI due to their intermedial character, while the aldehydes (e.g., MolID-44 and MolID-45) and carboxylates[72,73] (e.g., MolID-41 and MolID-42) have an overall chemically stabilizing effect that assists the passivation of the interphase with its liquid environment. The final performance parameter is the overall transport of Li^+ ions through the SEI during lithiation/delithiation cycles. The identity of the paramount Li conduction component of the SEI is still under debate;[74] however, recent work points to the importance of mixed-anion amorphous phases within the Li−O−P−F chemical space.[74,75] In particular, our recent computational study demonstrated that bulk amorphous $LiPO_2F_2$ (MolID-2) exhibits fast ionic conduction with exceptionally low Li-interstitial defect formation energies and rapid Li^+ diffusion, suggesting that mixed-anion Li−O−P−F phases can serve as primary Li-conducting channels within the SEI matrix.[74] Such regions within the SEI may be promoted by fluorinated phosphate−carbonate hybrids,[66,70,71] hydrogen bonding networks created by diols, and the polar groups found in ethers and linear carbonates. Confirming the specific role of each of these species in determining SEI performance remains an open challenge; nevertheless, this diverse molecular identification provides an unprecedented level of detail regarding the chemical makeup by which the overall interphase function is orchestrated. Additionally, the molecular detail provided here represents a critical step toward bridging the gap between electrolyte composition and SEI speciation. Because our framework resolves not only which species are present in the SEI but also how they emerge through specific decomposition pathways, it becomes possible to trace interphase components back to their molecular origins in the electrolyte. For example, formulations promoting coupled salt−solvent pathways can be pursued to favor the formation of fluorinated phosphate−carbonate hybrids that optimize the ionic transport. This ability to connect electrolyte composition to interphase speciation through mechanistically grounded pathways provides the chemical basis on which more deliberate and informed electrolyte development strategies can be built.

As stated earlier, these molecules were validated through exact mass matching with LDI-FTICR-MS, achieving mass accuracy to the fourth and fifth decimal places for species with molecular weights below and above $m/z = 175$, respectively. While this high-precision mass matching provides strong evidence for molecular presence, we acknowledge that mass spectrometry alone cannot definitively distinguish between structural isomers or confirm molecular connectivity (Figure S5). This study successfully demonstrates a joint computational−experimental methodology, with detailed structural validation representing an important avenue for future work. Expanding this approach to include complementary analytical techniques will significantly strengthen the reliability of SEI compositional assignments. Indeed, analytical techniques such as solid-state nuclear magnetic resonance (^{19}F, ^{31}P, ^{13}C, ^{7}Li) can directly probe local bonding environments, coordination states, and ionic mobility, allowing unambiguous differentiation between inorganic fluorophosphates, organophosphates, and carbonates. Furthermore, XPS provides valuable information on oxidation states and surface chemical environments, enabling quantification of the inorganic vs organic SEI fractions with high surface sensitivity. Moreover, vibrational spectroscopies such as FTIR and Raman offer complementary molecular fingerprints, ideal for confirming the presence of functional groups (e.g., P−O, C═O, C−O, and P−F motifs) predicted by computations. These techniques are particularly powerful for tracking polymeric or organic SEI components that are less accessible via XPS. Beyond surface analyses, to validate soluble or volatile byproducts, gas chromatography−mass spectrometry (GC MS) and liquid chromatography−mass spectrometry (LC MS), although primarily employed for direct electrolyte analysis, can also yield valuable insights into SEI chemistry. Because many SEI constituents originate from well-established electrolyte degradation pathways, the detection of soluble or volatile decomposition products provides indirect but meaningful information on the molecular species incorporated into the SEI. These techniques are therefore well suited for assessing the potentially soluble fraction of the SEI, identifying species that desorb, dissolve, or migrate into the electrolyte and would otherwise remain invisible to surface-focused analyses. Thus, following the example of Luo et al.,[76] who deciphered the detailed chemistry of the cathode−electrolyte interphase using a full dimensional analytical strategy, integrating such multi-technique validation within our computational−experimental framework represents a crucial direction for future research. Combining orthogonal structural, chemical, and spectroscopic signatures will greatly enhance the robustness and confidence of the SEI compositional analysis.

Furthermore, our eCRN models decomposition products to a defined computational depth, recognizing that the observed species (e.g., cyclic/bicyclic carbonates and other organic fragments) may undergo further reactions, including bond breaking, ring-opening, polymerization, cross-linking, etc., that extend beyond the current network boundaries. While our computational framework is limited to smaller molecules, experimental 2D mass defect analysis (Figure S6) reveals the presence of longer aliphatic carbon chains ($C_xH_yO_{1-5}$) with masses extending to 400−500 Da, indicating polymeric species beyond our computational predictions. These experimental signatures suggest that smaller species identified through the computational framework could undergo polymerization reactions during SEI formation to produce larger polymeric networks and highly condensed species. This is directly evidenced by the detection of poly(ethylene glycol) oligomers across the mass spectrum, where consecutive peaks are separated by exactly 44.02621 Da, corresponding to the C_2H_4O repeating unit (Figure S7 and Table S3). Finally, we acknowledge that our simulations do not incorporate explicit electrode surface effects on reaction pathways. Bin Jassar et al. showed that inorganic SEI surfaces can significantly alter reaction barriers and selectivity compared to gas-phase conditions.[77] Despite this limitation and given our uncertainty about the exact structure of the electrode surface, the agreement between our computational findings and experimental verifications highlights the strength of our computational framework. Our approach provides substantial value by narrowing the structural search space from infinite possibilities to well-defined computational candidates, transforming SEI characterization from empirical guessing into hypothesis-driven investigation guided by electrochemically plausible reaction pathways.

As previously discussed, our framework operates exclusively on thermodynamic data during the eCRN generation. Accordingly, the predicted mechanisms should be interpreted as candidate pathways that offer mechanistic explanations of the products. Each identified stable species may be formed through the predicted pathways, through alternative pathways not included in the species selection (e.g., by limiting the depth of fragmentation or recombination), or may not form in appreciable amounts due to kinetic hindrance in all possible pathways. The confirmation with LDI-FTICR-MS provided confidence that the proposed species are created in appreciable amounts, eliminating concerns about kinetic hindrance for the jointly observed species. However, without kinetic pathway validation, we cannot definitively establish which of the competing mechanistic routes will dominate under specific battery operating conditions, as even thermodynamically favorable processes can be rendered negligible if they encounter prohibitive activation barriers. While resolving the entire eCRN is currently beyond computational capabilities, we kinetically resolved the formation pathways for a representative set of molecules that were jointly observed by experiments and computation (Figure 7). All transition states below a 1 eV cutoff were deemed kinetically accessible, a practical threshold that reflects reactions under typical SEI formation conditions (room temperature to moderately elevated potentials). This cutoff also accounts for the evolving nature of the SEI, where species formed via higher barrier pathways are more prevalent in aged, high-cycle interfaces.

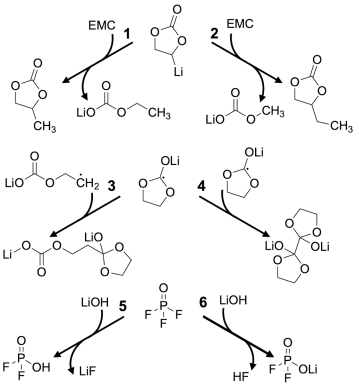

Reaction	$\Delta G^{\ddagger}$ [eV]	ΔG [eV]
1	0.63	−3.46
2	0.73	−3.25
3	0.10	−1.44
4	0.22	−1.79
5a	0.00	−1.52
5b	0.19	−0.07
6a	0.00	−1.27
6b	0.26	−0.29
6c	−0.01	−0.66

Figure 7. Possible routes for the formation of a representative set of molecules were jointly observed by experiments and computation. For multistep reactions such as reactions 5 and 6, a, b, and c represent sequential elementary steps (step 1, step 2, and step 3, respectively) with their corresponding activation energy barriers ($\Delta G^{\ddagger}$) and reaction free energies (ΔG) provided. Graphical snapshots of full energy diagram and relaxed structures (e.g., TSs) are depicted in Figures S9−S11.

The reactants in the included pathways are electrolyte starting components (EMC), previously kinetically resolved species (LiEC, POF_3, $Li^+EC\text{-}H^-$).[29,30,34] As shown in Figure 7, our calculations revealed that $Li^+EC\text{-}H^-$ (formed by replacing a hydrogen atom on the methylene group of EC with a Li atom) and EMC can undergo at least two distinct reaction pathways, each leading to different products. The first pathway proceeds via nucleophilic attack at the methyl carbon of EMC with an activation barrier of $\Delta G^{\ddagger} = 0.63$ eV, yielding propylene carbonate (MolID-10) and LEC (MolID-9) in a highly thermodynamically favorable process ($\Delta G = -3.46$ eV). The second pathway involves ethyl group transfer, proceeding through a 0.73 eV barrier to form 1,2-butylene carbonate (MolID-38) and LMC (MolID-8), with a reaction energy of −3.25 eV. Furthermore, reactions 3 and 4 represent competing pathways for the consumption of reduced LiEC. Reaction 3, between a ring opened and closed reduced LiEC, exhibits a low activation energy barrier of 0.10 eV, with substantial thermodynamic favorability ($\Delta G = -1.44$ eV), suggesting the rapid formation of lithium 2-(2-oxido-1,3-dioxolan-2-yl)ethyl carbonate (MolID-35) under typical battery operating conditions. The competing pathway (reaction 4) between two reduced LiEC molecules for the formation of lithium [2,2’-bi(1,3-dioxolane)]-2,2’-bis(olate) (MolID-50) requires a slightly higher kinetic barrier ($\Delta G^{\ddagger} = 0.22$ eV) with more favorable thermodynamic driving force ($\Delta G = -1.79$ eV).

Turning to the POF_3-mediated pathways in Figure 7, reaction 5a proceeds through a completely barrierless mechanism between POF_3 and LiOH ($\Delta G_a^{\ddagger} = 0.00$ eV) to form a PF_3OHOLi intermediate with a reaction energy of −1.52 eV. This intermediate then undergoes a simultaneous bond-breaking/bond-formation step with a minimal energy barrier of 0.19 eV. The second reaction is thermoneutral ($\Delta G_b = -0.07$ eV), but the reaction energy is calculated for LiF(solv), which is known to deposit LiF(s), a reaction reported to have a high driving force ($\Delta G = -1.17$ eV).[78] The absence of any significant kinetic barriers in this pathway indicates that the formation of LiF and difluorophosphoric acid occurs essentially instantaneously upon POF_3−LiOH contact. Notably, the formation of LiOH is usually associated with proton-transfer reactions as a result of hydrolysis or solvent decomposition products (see e.g. Figure S8).[79] Reaction 6 is a multistep mechanism leading to the formation of hydrogen fluoride (HF, MolID-26). After the formation of the PF_3OHOLi adduct, the O−H bond rotates with an activation barrier of $\Delta G_b^{\ddagger} = 0.26$ eV and a modest reaction energy of $\Delta G = -0.29$ eV. The subsequent bond-breaking bond-formation step (reaction 6c) to form HF and lithium phosphorodifluoridate (MolID-2) is barrierless ($\Delta G_c^{\ddagger} = -0.01$ eV), with a reaction energy of −0.66 eV. Overall, the parallel pathways highlighted in Figure 7 demonstrate a fundamental challenge in SEI prediction, where reactants can access multiple product channels depending on the local electrochemical environment, temperature, and other operating conditions. Consequently, the kinetic competition between these pathways determines the actual product distribution. Moreover, it is highly likely that additional pathways exist for other reactant combinations, particularly those involving radical intermediates or multimolecular cluster reactions that were not captured in our two-body analysis. For example, the chemical potentials of radical species such as H* and F* are highly sensitive to the local environment and therefore render the reaction energetics context-dependent. This underscores the importance of observing the same products in the mass spectrometry data. In general, we can only claim that these are some of the possible ways that these species are formed. Further work should be done to gain more confidence in which pathways dominate the formation of specific species. This would require comprehensive kinetic modeling that accounts for pathway competition, intermediate stability, and the influence of local electrochemical potential on reaction barriers. Only through this more rigorous analysis may we gain the knowledge necessary to make mechanistically informed decisions regarding changes to the electrolyte’s initial composition.

Looking forward, the integration of machine learning interatomic potentials (MLIPs) with species selection represents an opportunity to overcome the current computational bottlenecks that limit kinetic analysis to small subsets of reactions. While our detailed kinetic refinement has revealed critical mechanistic insights into key pathways, the generated reaction network contains millions of potential reactions that remain kinetically unresolved. The development of MLIPs trained on high-quality DFT transition state data could enable rapid estimation of activation barriers across the entire reaction network, finally bridging the gap between thermodynamic feasibility and kinetic accessibility that currently limits eCRN predictive power. Recent advances in universal MLIPs and automated transition state search algorithms suggest that such an approach could computationally screen millions of elementary steps at near-DFT accuracy within practical timeframes.[80,81] Alternatively, physics-based semiempirical methods offer orders of magnitude computational speedup over DFT.[82] However, it is essential to note that these methods require ongoing validation, reparameterization, and careful benchmarking due to their reliance on approximations and empirical data rather than purely first-principles calculations. By leveraging automated eCRN generation and stochastic network analysis, future frameworks could uncover new reaction pathways, identify key intermediates, and improve the reliability of kinetic models used in a variety of applications from reactor design, emissions control, electrochemical devices, to plastics degradation and fuel optimization. Finally, future studies should move beyond compositional identification to determine whether individual SEI species contribute to beneficial or detrimental interphase functionality. As recently demonstrated,[74] a promising strategy is to leverage emerging generative AI approaches to transform identified SEI fragments into bulk analogs that preserve key molecular motifs and then evaluate their intrinsic ionic conductivity, electronic insulation, and mechanical properties. This function-centric mapping from species to material properties provides a pathway to rationally classify SEI components and guide the design of stable, high-performance interphases.

■ CONCLUSIONS

In this work, we provided a comprehensive molecular-level characterization of the SEI formed on graphite in a carbonate-based Li-ion battery electrolyte through the integration of ultrahigh-resolution LDI-FTICR-MS, data-driven electrochemical reaction networks, and stochastic simulations. The synergetic combination of these simulations and high-resolution experimental techniques leads to the identification of new molecular species with high confidence. We generated the largest and most comprehensive eCRN for SEI formation in LIBs, consisting of over 10,000 species and 209 million reactions. Stochastic network analysis yielded many known SEI components, as well as novel species that had not previously been proposed. These newly identified molecules were validated with LDI-FTICR-MS and spanned diverse structural motifs including fluorinated organophosphate−carbonates, cyclic and bicyclic alkyl carbonates, carboxylates, diols, formates, oxalates, dioxolanes, and ethers that collectively expand our understanding of SEI chemical diversity. Kinetic analysis of formation pathways for a set of representative molecules revealed kinetically feasible routes with activation energy barriers, ranging from completely barrierless to less than 1.0 eV. Together, this work establishes a molecular and mechanistic foundation that connects electrolyte composition to SEI speciation, advancing the community's ability to develop more stable, efficient, and longer-lasting lithium-based energy storage systems.

■ ASSOCIATED CONTENT

Supporting Information

The Supporting Information is available free of charge at https://pubs.acs.org/doi/10.1021/jacs.6c04755.

> Formation cycle of NMC/graphite pouch cells; first-cycle capacity data; FTICR-MS of four negative graphite electrodes for the formation cycle; FTICR-MS of the cycled graphite electrode; species and reactions filters; FTICR-MS molecular assignment for all novel species; structural comparison of isomers with similar *m*/*z*; 2D mass spectrum representation mapping of SEI species for the formation cycle and after 250 cycles; energy diagrams for the formation pathways of selected SEI species (PDF)
>
> JSON file containing structural, thermodynamic, and vibrational information on all molecules in this work (ZIP)

■ AUTHOR INFORMATION

Corresponding Author

Kristin A. Persson — *Bakar Institute of Digital Materials for the Planet and Department of Materials Science and Engineering, University of California at Berkeley, Berkeley, California 94720, United States; Materials Science Division, Lawrence Berkeley National Laboratory, Berkeley, California 94720, United States;* orcid.org/0000-0003-2495-5509; Email: kristinpersson@berkeley.edu

Authors

Mona Abdelgaid — *Bakar Institute of Digital Materials for the Planet, University of California at Berkeley, Berkeley, California 94720, United States; Materials Science Division, Lawrence Berkeley National Laboratory, Berkeley, California 94720, United States;* orcid.org/0000-0003-0973-3262

Oliver Hvidsten — *Materials Science Division, Lawrence Berkeley National Laboratory, Berkeley, California 94720, United States; Department of Materials Science and Engineering, University of California at Berkeley, Berkeley, California 94720, United States*

Théo Sombret — *INSA Rouen Normandie, Université de Caen Normandie, ENSICAEN, CNRS, Institut CARMeN UMR 6064, Université de Rouen Normandie, Cedex F-76821 Mont-Saint-Aignan, France; TotalEnergies Research and Technology Gonfreville, TotalEnergies OneTech, 76700 Harfleur, France; Corporate Research, Saft, 33074 Bordeaux, France; International Joint Laboratory-Complex Matrices Molecular Characterization (iC2MC), TRTG, 76700 Harfleur, France*

Egon Kherchiche — *INSA Rouen Normandie, Université de Caen Normandie, ENSICAEN, CNRS, Institut CARMeN UMR 6064, Université de Rouen Normandie, Cedex F-76821 Mont-Saint-Aignan, France; TotalEnergies Research and Technology Gonfreville, TotalEnergies OneTech, 76700 Harfleur, France; Corporate Research, Saft, 33074 Bordeaux, France; International Joint Laboratory-Complex Matrices Molecular Characterization (iC2MC), TRTG, 76700 Harfleur, France*

Julien Maillard — *TotalEnergies Research and Technology Gonfreville, TotalEnergies OneTech, 76700 Harfleur, France; International Joint Laboratory-Complex Matrices Molecular Characterization (iC2MC), TRTG, 76700 Harfleur, France*

Antonin Gajan — *Corporate Research, Saft, 33074 Bordeaux, France*

Patrick Bernard — *Corporate Research, Saft, 33074 Bordeaux, France*

Kamila Kaźmierczak — *TotalEnergies OneTech Belgium, 7181 Seneffe, Belgium*

Mauricio Araya-Polo — *TotalEnergies EP Research and Technology, Houston, Texas 77002, United States*

Germain Salvato Vallverdu — *International Joint Laboratory-Complex Matrices Molecular Characterization (iC2MC), TRTG, 76700 Harfleur, France; IPREM, Université de Pau et des Pays de l'Adour, CNRS, 64000 Pau, France;* orcid.org/0000-0003-1116-8776

Carlos Afonso — *INSA Rouen Normandie, Université de Caen Normandie, ENSICAEN, CNRS, Institut CARMeN UMR 6064, Université de Rouen Normandie, Cedex F-76821 Mont-Saint-Aignan, France; International Joint Laboratory-Complex Matrices Molecular Characterization (iC2MC), TRTG, 76700 Harfleur, France;* orcid.org/0000-0002-2406-5664

Pierre Giusti — *TotalEnergies Research and Technology Gonfreville, TotalEnergies OneTech, 76700 Harfleur, France; International Joint Laboratory-Complex Matrices Molecular Characterization (iC2MC), TRTG, 76700 Harfleur, France; INSA Rouen Normandie, Université de Caen Normandie, ENSICAEN, CNRS, Institut CARMeN UMR 6064, Université de Rouen Normandie, Cedex F-76821 Mont-Saint-Aignan, France;* orcid.org/0000-0002-9569-3158

Complete contact information is available at: https://pubs.acs.org/10.1021/jacs.6c04755

Notes

The authors declare no competing financial interest.

■ ACKNOWLEDGMENTS

This work was supported by a research grant from TotalEnergies to the University of California, Berkeley. M.A. acknowledges funding support from the Bakar Institute of Digital Materials for the Planet Postdoctoral Fellowship. The research was performed using computational resources sponsored by the Department of Energy's Office of Critical Minerals and Energy Innovation and located at the National Laboratory of the Rockies. This research also used the Lawrencium computational cluster resource provided by the IT Division at the Lawrence Berkeley National Laboratory (supported by the Director, Office of Science, Office of Basic Energy Sciences, of the U.S. Department of Energy under Contract No. DE-AC02-05CH11231). Schrödinger, Inc. provided access to Jaguar and AutoTS software. C.A. acknowledges financial support from Labex SynOrg (ANR-11-LABX-0029) and the CNRS research infrastructure Infranalytics (FR2054) for instrument time.

■ REFERENCES

(1) Kim, T.-H.; Park, J.-S.; Chang, S. K.; Choi, S.; Ryu, J. H.; Song, H.-K. The Current Move of Lithium Ion Batteries Towards the Next Phase. *Adv. Energy Mater.* **2012**, 2 (7), 860−872.

(2) Darga, J.; Lamb, J.; Manthiram, A. Industrialization of Layered Oxide Cathodes for Lithium-Ion and Sodium-Ion Batteries: A Comparative Perspective. *Energy Technology* **2020**, *8* (12), No. 2000723.

(3) Cheng, X.-B.; Zhang, R.; Zhao, C.-Z.; Wei, F.; Zhang, J.-G.; Zhang, Q. A Review of Solid Electrolyte Interphases on Lithium Metal Anode. *Adv. Sci.* **2016**, *3*, 1500213.

(4) Hasan, M.M.; Haque, R.; Jahirul, M.I.; Rasul, M.G.; Fattah, I.M.R.; Hassan, N.M.S.; Mofijur, M. Advancing Energy Storage: The Future Trajectory of Lithium-Ion Battery Technologies. *J. Energy Storage* **2025**, *120*, No. 116511.

(5) Peled, E. The Electrochemical Behavior of Alkali and Alkaline Earth Metals in Nonaqueous Battery Systems—The Solid Electrolyte Interphase Model. *J. Electrochem. Soc.* **1979**, *126* (12), 2047.

(6) Verma, P.; Maire, P.; Novak, P. A review of the features and analyses of the solid electrolyte interphase in Li-ion batteries. *Electrochim. Acta.* **2010**, *55* (22), 6332−6341.

(7) Cheng, X.; Zhang, R.; Zhao, C.; Wei, F.; Zhang, J.; Zhang, Q. A Review of Solid Electrolyte Interphases on Lithium Metal Anode. *Adv. Sci.* **2016**, *3* (3), No. 1500213.

(8) Peled, E.; Menkin, S. Review-SEI: Past, Present and Future. *J. Electrochem. Soc.* **2017**, *164* (7), A1703−A1719.

(9) Winter, M. The Solid Electrolyte Interphase − The Most Important and the Least Understood Solid Electrolyte in Rechargeable Li Batteries. *Z. Phys. Chem.* **2009**, *223* (10−11), 1395−1406.

(10) Freunberger, S. A. Interphase Identity Crisis. *Nat. Chem.* **2019**, *11* (9), 761−763.

(11) Wu, J.; Ihsan-Ul-Haq, M.; Chen, Y.; Kim, J.-K. Understanding Solid Electrolyte Interphases: Advanced Characterization Techniques and Theoretical Simulations. *Nano energy* **2021**, *89*, No. 106489.

(12) Leroy, S.; Martinez, H.; Dedryvère, R.; Lemordant, D.; Gonbeau, D. Influence of the Lithium Salt Nature over the Surface Film Formation on a Graphite Electrode in Li-Ion Batteries: An XPS Study. *Appl. Surf. Sci.* **2007**, *253* (11), 4895−4905.

(13) Harks, P. P. R. M. L.; Mulder, F. M.; Notten, P. H. L. In Situ Methods for Li-Ion Battery Research: A Review of Recent Developments. *J. Power Sources* **2015**, *288*, 92−105.

(14) Pekarek, R. T.; Affolter, A.; Baranowski, L. L.; Coyle, J.; Hou, T.; Sivonxay, E.; Smith, B. A.; McAuliffe, R. D.; Persson, K. A.; Key, B.; Apblett, C.; Veith, G. M.; Neale, N. R. Intrinsic Chemical Reactivity of Solid-Electrolyte Interphase Components in Silicon−Lithium Alloy Anode Batteries Probed by FTIR Spectroscopy. *J. Mater. Chem. A* **2020**, *8* (16), 7897−7906.

(15) Gauthier, N.; Courrèges, C.; Demeaux, J.; Tessier, C.; Martinez, H. Probing the In-Depth Distribution of Organic/Inorganic Molecular Species within the SEI of LTO/NMC and LTO/LMO Batteries: A Complementary ToF-SIMS and XPS Study. *Appl. Surf. Sci.* **2020**, *501*, No. 144266.

(16) Huang, Z.; Tian, R.; Gao, Y. The review of time of flight secondary ion mass spectrometry technology in LIBs. *Int. J. Mass Spectrom.* **2026**, *521*, 117584.

(17) Shan, X.; Zhong, Y.; Zhang, L.; Zhang, Y.; Xia, X.; Wang, X.; Tu, J. A Brief Review on Solid Electrolyte Interphase Composition Characterization Technology for Lithium Metal Batteries: Challenges and Perspectives. *J. Phys. Chem. C* **2021**, *125* (35), 19060−19080.

(18) Wood, K. N.; Teeter, G. XPS on Li-Battery-Related Compounds: Analysis of Inorganic SEI Phases and a Methodology for Charge Correction. *ACS Appl. Energy Mater.* **2018**, *1* (9), 4493−4504.

(19) Bak, S.-M.; Shadike, Z.; Lin, R.; Yu, X.; Yang, X.-Q. In Situ/Operando Synchrotron-Based X-Ray Techniques for Lithium-Ion Battery Research. *NPG Asia Materials* **2018**, *10* (7), 563−580.

(20) Shutthanandan, V.; Nandasiri, M.; Zheng, J.; Engelhard, M. H.; Xu, W.; Thevuthasan, S.; Murugesan, V. Applications of XPS in the Characterization of Battery Materials. *J. Electron Spectrosc. Relat. Phenom.* **2019**, *231*, 2−10.

(21) Comisarow, M. B.; Marshall, A. G. Fourier Transform Ion Cyclotron Resonance Spectroscopy. *Chem. Phys. Lett.* **1974**, *25* (2), 282−283.

(22) Hendrickson, C. L.; Quinn, J. P.; Kaiser, N. K.; Smith, D. F.; Blakney, G. T.; Chen, T.; Marshall, A. G.; Weisbrod, C. R.; Beu, S. C. 21 T Fourier Transform Ion Cyclotron Resonance Mass Spectrometer: A National Resource for Ultrahigh Resolution Mass Analysis. *J. Am. Soc. Mass Spectrom.* **2015**, *26* (9), 1626−1632.

(23) Maillard, J.; Carrasco, N.; Schmitz-Afonso, I.; Gautier, T.; Afonso, C. Comparison of Soluble and Insoluble Organic Matter in Analogues of Titan's Aerosols. *Earth and Planetary Science Letters* **2018**, *495*, 185−191.

(24) Krajewski, L. C.; Rodgers, R. P.; Marshall, A. G. 126 264 Assigned Chemical Formulas from an Atmospheric Pressure Photoionization 9.4 T Fourier Transform Positive Ion Cyclotron Resonance Mass Spectrum. *Anal. Chem.* **2017**, *89* (21), 11318−11324.

(25) Miladinović, S. M.; Kozhinov, A. N.; Gorshkov, M. V.; Tsybin, Y. O. On the Utility of Isotopic Fine Structure Mass Spectrometry in Protein Identification. *Anal. Chem.* **2012**, *84* (9), 4042−4051.

(26) Ferey, J.; Larroque, M.; Schmitz-Afonso, I.; Le Maître, J.; Sgarbura, O.; Carrere, S.; Quenet, F.; Bouyssiere, B.; Enjalbal, C.; Mounicou, S.; Afonso, C. Imaging Matrix-Assisted Laser Desorption/Ionization Fourier Transform Ion Cyclotron Resonance Mass Spectrometry of Oxaliplatin Derivatives in Human Tissue Sections. *Talanta* **2022**, *237*, No. 122915.

(27) Maillard, J. F.; Demeaux, J.; Mase, C.; Gajan, A.; Tessier, C.; Bernard, P.; Afonso, C.; Giusti, P. Unambiguous Molecular Characterization of Solid Electrolyte Interphase Species on Graphite Negative Electrodes. *J. Power Sources* **2023**, *582*, No. 233516.

(28) Sombret, T.; Kherchiche, E.; Hubert-Roux, M.; Gajan, A.; Maillard, J.; Afonso, C.; Giusti, P. Matrix-Assisted Laser Desorption Ionization Mass Spectrometry: An Efficient Approach to Monitor Lithium-Ion Battery Electrolyte Degradation While Preserving Analyte Integrity. *J. Am. Soc. Mass Spectrom.* **2025**, *36* (7), 1553−1560.

(29) Xie, X.; Clark Spotte-Smith, E. W.; Wen, M.; Patel, H. D.; Blau, S. M.; Persson, K. A. Data-Driven Prediction of Formation Mechanisms of Lithium Ethylene Monocarbonate with an Automated Reaction Network. *J. Am. Chem. Soc.* **2021**, *143* (33), 13245−13258.

(30) Barter, D.; Spotte-Smith, E. W.; Redkar, N. S.; Khanwale, A.; Dwaraknath, S.; Persson, K. A.; Blau, S. M. Predictive Stochastic Analysis of Massive Filter-Based Electrochemical Reaction Networks. *Digital Discovery* **2023**, *2* (1), 123−137.

(31) Spotte-Smith, E. W. C.; Kam, R. L.; Barter, D.; Xie, X.; Hou, T.; Dwaraknath, S.; Blau, S. M.; Persson, K. A. Toward a Mechanistic Model of Solid−Electrolyte Interphase Formation and Evolution in Lithium-Ion Batteries. *ACS Energy Lett.* **2022**, *7* (4), 1446−1453.

(32) Blau, S. M.; Patel, H. D.; Spotte-Smith, E. W. C.; Xie, X.; Dwaraknath, S.; Persson, K. A. A Chemically Consistent Graph Architecture for Massive Reaction Networks Applied to Solid-Electrolyte Interphase Formation. *Chem. Sci.* **2021**, *12* (13), 4931−4939.

(33) Bin Jassar, M.; De Bruin, T.; Nieto-Draghi, C.; Steinmann, S. N. Challenges and Opportunities in Using Kinetic Monte Carlo for Battery Research and Innovation. *EES Batteries* **2025**, *1* (4), 788−802.

(34) Spotte-Smith, E. W. C.; Petrocelli, T. B.; Patel, H. D.; Blau, S. M.; Persson, K. A. Elementary Decomposition Mechanisms of Lithium Hexafluorophosphate in Battery Electrolytes and Interphases. *ACS Energy Lett.* **2023**, *8* (1), 347−355.

(35) Spotte-Smith, E. W. C.; Blau, S. M.; Xie, X.; Patel, H. D.; Wen, M.; Wood, B.; Dwaraknath, S.; Persson, K. A. Quantum Chemical Calculations of Lithium-Ion Battery Electrolyte and Interphase Species. *Scientific Data* **2021**, *8* (1), 203.

(36) Kong, J.; White, C. A.; Krylov, A. I.; Sherrill, D.; Adamson, R. D.; Furlani, T. R.; Lee, M. S.; Lee, A. M.; Gwaltney, S. R.; Adams, T. R.; Ochsenfeld, C.; Gilbert, A. T. B.; Kedziora, G. S.; Rassolov, V. A.; Maurice, D. R.; Nair, N.; Shao, Y.; Besley, N. A.; Maslen, P. E.; Dombroski, J. P.; Daschel, H.; Zhang, W.; Korambath, P. P.; Baker, J.; Byrd, E. F. C.; Van Voorhis, T.; Oumi, M.; Hirata, S.; Hsu, C.-P.; Ishikawa, N.; Florian, J.; Warshel, A.; Johnson, B. G.; Gill, P. M. W.; Head-Gordon, M.; Pople, J. A. Q-Chem 2.0: A High-Performance Ab Initio Electronic Structure Program Package. *J. Comput. Chem.* **2000**, *21* (16), 1532−1548.

(37) Mardirossian, N.; Head-Gordon, M. ωB97X-V: A 10-Parameter, Range-Separated Hybrid, Generalized Gradient Approximation Density Functional with Nonlocal Correlation, Designed by a Survival-of-the-Fittest Strategy. *Phys. Chem. Chem. Phys.* **2014**, *16* (21), 9904−9924.

(38) Weigend, F.; Ahlrichs, R. Balanced Basis Sets of Split Valence, Triple Zeta Valence and Quadruple Zeta Valence Quality for H to Rn: Design and Assessment of Accuracy. *Physical chemistry chemical physics: PCCP* **2005**, *7* (18), 3297−3305.

(39) Marenich, A. V.; Cramer, C. J.; Truhlar, D. G. Universal Solvation Model Based on Solute Electron Density and on a Continuum Model of the Solvent Defined by the Bulk Dielectric Constant and Atomic Surface Tensions. *J. Phys. Chem. B* **2009**, *113* (18), 6378−6396.

(40) Jacobson, L. D.; Bochevarov, A. D.; Watson, M. A.; Hughes, T. F.; Rinaldo, D.; Ehrlich, S.; Steinbrecher, T. B.; Vaitheeswaran, S.; Philipp, D. M.; Halls, M. D.; Friesner, R. A. Automated Transition State Search and Its Application to Diverse Types of Organic Reactions. *J. Chem. Theory Comput.* **2017**, *13* (11), 5780−5797.

(41) Bochevarov, A. D.; Harder, E.; Hughes, T. F.; Greenwood, J. R.; Braden, D. A.; Philipp, D. M.; Rinaldo, D.; Halls, M. D.; Zhang, J.; Friesner, R. A. Jaguar: A High-Performance Quantum Chemistry Software Program with Strengths in Life and Materials Sciences. *International journal of quantum chemistry* **2013**, *113* (18), 2110−2142.

(42) Chai, J.-D.; Head-Gordon, M. Long-Range Corrected Hybrid Density Functionals with Damped Atom−Atom Dispersion Corrections. *Physical chemistry chemical physics: PCCP* **2008**, *10* (44), 6615−6620.

(43) Rappoport, D.; Furche, F. Property-Optimized Gaussian Basis Sets for Molecular Response Calculations. *J. Chem. Phys.* **2010**, *133* (13), 134105−134111.

(44) Barone, V.; Cossi, M. Quantum Calculation of Molecular Energies and Energy Gradients in Solution by a Conductor Solvent Model. *J. Phys. Chem. A* **1998**, *102* (11), 1995−2001.

(45) Maeda, S.; Harabuchi, Y.; Ono, Y.; Taketsugu, T.; Morokuma, K. Intrinsic Reaction Coordinate: Calculation, Bifurcation, and Automated Search. *Int. J. Quantum Chem.* **2015**, *115* (5), 258−269.

(46) Klamt, A.; Schüürmann, G. COSMO: A New Approach to Dielectric Screening in Solvents with Explicit Expressions for the Screening Energy and Its Gradient. *J. Chem. Soc., Perkin Trans.* **1993**, *2* (5), 799−805.

(47) Zichi, L.; Barter, D.; Sivonxay, E.; Spotte-Smith, E. W. C.; Mohanakrishnan, R. S.; Chan, E. M.; Persson, K. A.; Blau, S. M. RNMC: Kinetic Monte Carlo Implementations for Complex Reaction Networks. *Journal of open source software* **2024**, *9* (104), 7244.

(48) Gillespie, D. T. A General Method for Numerically Simulating the Stochastic Time Evolution of Coupled Chemical Reactions. *J. Comput. Phys.* **1976**, *22* (4), 403−434.

(49) Stocker, S.; Csányi, G.; Reuter, K.; Margraf, J. T. Machine Learning in Chemical Reaction Space. *Nat. Commun.* **2020**, *11* (1), 5505.

(50) Rowden, B.; Garcia-Araez, N. A Review of Gas Evolution in Lithium Ion Batteries. *Energy Reports* **2020**, *6*, 10−18.

(51) Verma, P.; Maire, P.; Novák, P. A Review of the Features and Analyses of the Solid Electrolyte Interphase in Li-Ion Batteries. *Electrochim. Acta* **2010**, *55* (22), 6332−6341.

(52) Rinkel, B. L. D.; Hall, D. S.; Temprano, I.; Grey, C. P. Electrolyte Oxidation Pathways in Lithium-Ion Batteries. *J. Am. Chem. Soc.* **2020**, *142* (35), 15058−15074.

(53) Liu, C.; Ren, K.; Wu, S.; Zhang, Y.; Li, H.-W.; Yao, M.; Jiang, Z.; Li, Y. Reevaluating the Effect of a LiF-Containing Solid Electrolyte Interphase on Lithium Metal Anodes. *Nano Lett.* **2025**, *25* (19), 7762−7769.

(54) Parimalam, B. S.; MacIntosh, A. D.; Kadam, R.; Lucht, B. L. Decomposition Reactions of Anode Solid Electrolyte Interphase (SEI) Components with LiPF6. *J. Phys. Chem. C* **2017**, *121* (41), 22733−22738.

(55) Adenusi, H.; Chass, G. A.; Passerini, S.; Tian, K. V.; Chen, G. Lithium Batteries and the Solid Electrolyte Interphase (SEI)—Progress and Outlook. *Adv. Energy Mater.* **2023**, *13* (10), 2203307.

(56) Henschel, J.; Peschel, C.; Klein, S.; Horsthemke, F.; Winter, M.; Nowak, S. Clarification of Decomposition Pathways in a State-of-the-Art Lithium Ion Battery Electrolyte through 13C-Labeling of Electrolyte Components. *Angew. Chem., Int. Ed.* **2020**, *59* (15), 6128−6137.

(57) Smith, K.; Gasper, P.; Colclasure, A. M.; Shimonishi, Y.; Yoshida, S. Lithium-Ion Battery Life Model with Electrode Cracking and Early-Life Break-in Processes. *J. Electrochem. Soc.* **2021**, *168* (10), 100530.

(58) Kawaura, H.; Harada, M.; Kondo, Y.; Mizutani, M.; Takahashi, N.; Yamada, N. L. Effects of Lithium Bis(Oxalate)Borate Electrolyte Additive on the Formation of a Solid Electrolyte Interphase on Amorphous Carbon Electrodes by Operando Time-Slicing Neutron Reflectometry. *ACS Appl. Mater. Interfaces* **2022**, *14* (21), 24526−24535.

(59) Wang, X.; Li, C.; Chen, Z.; Sun, Y. Implantation of Solid Electrolyte Interphase Stabilizer within High-Capacity Silicon Electrode Enabling Enhanced Battery Performance. *Energy Material Advances* **2024**, *5*, No. 0095.

(60) Huang, S.; Wang, S.; Hu, G.; Cheong, L.-Z.; Shen, C. Modulation of Solid Electrolyte Interphase of Lithium-Ion Batteries by LiDFOB and LiBOB Electrolyte Additives. *Appl. Surf. Sci.* **2018**, *441*, 265−271.

(61) Yang, Y.; Xiong, J.; Lai, S.; Zhou, R.; Zhao, M.; Geng, H.; Zhang, Y.; Fang, Y.; Li, C.; Zhao, J. Vinyl Ethylene Carbonate as an Effective SEI-Forming Additive in Carbonate-Based Electrolyte for Lithium-Metal Anodes. *ACS Appl. Mater. Interfaces* **2019**, *11* (6), 6118−6125.

(62) Li, J.; Yao, W.; Meng, Y. S.; Yang, Y. Effects of Vinyl Ethylene Carbonate Additive on Elevated-Temperature Performance of Cathode Material in Lithium Ion Batteries. *J. Phys. Chem. C* **2008**, *112* (32), 12550−12556.

(63) Chai, J.; Liu, Z.; Ma, J.; Wang, J.; Liu, X.; Liu, H.; Zhang, J.; Cui, G.; Chen, L. In Situ Generation of Poly (Vinylene Carbonate) Based Solid Electrolyte with Interfacial Stability for LiCoO2 Lithium Batteries. *Advanced Science* **2017**, *4* (2), 1600377.

(64) Jankowski, P.; Wieczorek, W.; Johansson, P. SEI-Forming Electrolyte Additives for Lithium-Ion Batteries: Development and Benchmarking of Computational Approaches. *J. Mol. Model* **2017**, *23* (1), 6.

(65) Park, S.; Jeong, S. Y.; Lee, T. K.; Park, M. W.; Lim, H. Y.; Sung, J.; Cho, J.; Kwak, S. K.; Hong, S. Y.; Choi, N.-S. Replacing Conventional Battery Electrolyte Additives with Dioxolone Derivatives for High-Energy-Density Lithium-Ion Batteries. *Nat. Commun.* **2021**, *12* (1), 838.

(66) Hu, A.; Liao, Z.; Yang, Q.; Huang, J.; Wei, Z.; Sun, Y.; Zhao, E.; Zhang, Z.; Yang, L.; Saito, N.; Orita, A. Interphase Optimum via Synergistic Effect of Poly(1,3-Dioxolane) Electrolytes and Lithium Difluorophosphate for Stable Lithium Metal Batteries. *Adv. Funct. Mater.* **2024**, *34* (51), 2410282.

(67) Santhosh, P.; Vasudevan, T.; Gopalan, A.; Lee, K.-P. Preparation and Properties of New Cross-Linked Polyurethane Acrylate Electrolytes for Lithium Batteries. *J. Power Sources* **2006**, *160* (1), 609−620.

(68) Chen, X.; Yi, L.; Zou, C.; Liu, J.; Yang, L.; Zang, Z.; Tao, X.; Luo, Z.; Chang, B.; Shen, Y.; Wang, X. Boosting the Performances of Lithium Metal Batteries through In-Situ Construction of Dual-Network Self-Healing Gel Polymer Electrolytes. *Electrochim. Acta* **2023**, *446*, No. 142084.

(69) Bouguern, M. D.; M R, A. K.; Zaghib, K. The Critical Role of Interfaces in Advanced Li-Ion Battery Technology: A Comprehensive Review. *J. Power Sources* **2024**, *623*, No. 235457.

(70) Fan, X.; Ji, X.; Han, F.; Yue, J.; Chen, J.; Chen, L.; Deng, T.; Jiang, J.; Wang, C. Fluorinated Solid Electrolyte Interphase Enables Highly Reversible Solid-State Li Metal Battery. *Science Advances* **2018**, *4* (12), No. eaau9245.

(71) Kim, M.-H.; Wi, T.-U.; Seo, J.; Choi, A.; Ko, S.; Kim, J.; Jung, U.; Kim, M. S.; Park, C.; Jin, S.; Lee, H.-W. Design Principles for Fluorinated Interphase Evolution via Conversion-Type Alloying Processes for Anticorrosive Lithium Metal Anodes. *Nano Lett.* **2023**, *23* (8), 3582−3591.

(72) Jeschull, F.; Zhang, L.; Kondracki, Ł.; Scott, F.; Trabesinger, S. Interphase Formation with Carboxylic Acids as Slurry Additives for Si

Electrodes in Li-Ion Batteries. Part 1: Performance and Gas Evolution. *Journal of Physics: Energy* **2023**, *5* (2), No. 025003.

(73) Nogales, P. M.; Lee, S.; Yang, S.; Jeong, S.-K. Effects of Electrolyte Solvent Composition on Solid Electrolyte Interphase Properties in Lithium Metal Batteries: Focusing on Ethylene Carbonate to Ethyl Methyl Carbonate Ratios. *Batteries* **2024**, *10* (6), 210.

(74) Zhong, P.; Persson, K. A. Machine-Learning-Guided Insights into Solid-Electrolyte Interphase Conductivity: Are Amorphous Lithium Fluorophosphates the Key? *ACS Energy Lett.* **2026**, *11* (1), 806−812.

(75) Liu, X.; Li, S.; Yuan, C.; Zheng, B.; Cheng, G.; Chen, Y.; Lu, X.; Gu, D.; Lv, B.; Li, H.; Yan, Z.; Qian, H.; Zhu, Y.; Sun, D.; Song, Y.; Xiang, Y. Probing the Heterogeneous Nature of LiF in Solid−Electrolyte Interphases. *Nature* **2025**, *646* (8083), 102−107.

(76) Luo, H.; Zhang, B.; Zhang, H.; Zheng, Q.; Wu, X.; Yan, Y.; Li, Z.; Tang, Y.; Hao, W.; Liu, G.; Hong, Y.; Ye, J.; Qiao, Y.; Sun, S.-G. Full-Dimensional Analysis of Electrolyte Decomposition on Cathode−Electrolyte Interface: Establishing Characterization Paradigm on LiNi0.6Co0.2Mn0.2O2 Cathode with Potential Dependence. *J. Phys. Chem. Lett.* **2023**, *14* (19), 4565−4574.

(77) Bin Jassar, M.; Michel, C.; Abada, S.; De Bruin, T.; Tant, S.; Nieto-Draghi, C.; Steinmann, S. N. A Joint DFT-kMC Study To Model Ethylene Carbonate Decomposition Reactions: SEI Formation, Growth, and Capacity Loss during Calendar Aging of Li-Metal Batteries. *ACS Appl. Energy Mater.* **2023**, *6* (13), 6934−6945.

(78) Okamoto, Y. Ab Initio Calculations of Thermal Decomposition Mechanism of LiPF6-Based Electrolytes for Lithium-Ion Batteries. *J. Electrochem. Soc.* **2013**, *160* (2), A404.

(79) Di Muzio, S.; Paolone, A.; Brutti, S. Thermodynamics of the Hydrolysis of Lithium Salts: Pathways to the Precipitation of Inorganic SEI Components in Li-Ion Batteries. *J. Electrochem. Soc.* **2021**, *168* (10), 100514.

(80) Liu, Y.; Morrow, J. D.; Ertural, C.; Fragapane, N. L.; Gardner, J. L. A.; Naik, A. A.; Zhou, Y.; George, J.; Deringer, V. L. An Automated Framework for Exploring and Learning Potential-Energy Surfaces. *Nat. Commun.* **2025**, *16* (1), 7666.

(81) Achar, S. K.; Shukla, P. B.; Mhatre, C. V.; Bernasconi, L.; Vinger, C. Y.; Johnson, J. K. Reactive Active Learning: An Efficient Approach for Training Machine Learning Interatomic Potentials for Reacting Systems. *J. Chem. Theory Comput.* **2025**, *21* (18), 8889−8906.

(82) Bin Jassar, M.; Michel, C.; Abada, S.; De Bruin, T.; Tant, S.; Nieto-Draghi, C.; Steinmann, S. N. Lessons Learned from Semi-empirical Methods for the Li-Ion Battery Solid Electrolyte Interphase. *J. Phys. Chem. C* **2024**, *128* (8), 3269−3280.